Development of icy regolith simulant for lunar permanently shadowed regions

Kārlis Šļumba [a,b,*], Hannah M. Sargeant [a,1], Daniel T. Britt [a,b]

[a] *University of Central Florida, Department of Physics, 4111 Libra Dr., PSB430, Orlando, FL 32816, USA*
[b] *Exolith Lab, 532 South Econ Cir, Oviedo, FL 32765, USA*

Abstract

The lunar poles are thought to contain vast ice deposits that could be beneficial to future space exploration efforts. However, it is not well characterized how water ice content affects regolith and dust physical properties. In order to develop suitable technologies that can operate safely in the cryogenic regolith, testing should be conducted in simulated regolith. We present a new production method for lunar permanently shadowed regions (PSRs) icy regolith simulant. We build on an existing lunar highlands simulant, by adapting it for lunar poles, where water ice might be present in PSRs. We have demonstrated a production concept using controllable simulant and water flow rates to make granular icy simulant with variable water ice content. We found that with this production method, icy simulant has a porosity of 0.6 to 0.7, that persists even after dehydration.
© 2024 COSPAR. Published by Elsevier B.V. This is an open access article under the CC BY license (http://creativecommons.org/licenses/by/4.0/).

1. Introduction

Planetary science has gained a new wave of enthusiasm with the NASA Artemis missions that will take humans back to the lunar surface. The Artemis program plans to take astronauts to the lunar south pole, where surface properties might be very different from equatorial regions previously visited by Apollo astronauts, for example, regolith bearing capacity seems to be somewhat lower in permanently shadowed regions (PSRs) (Sargeant et al., 2020). Also, because of the Moon's low inclination, some craters near the poles never see sunlight, these are called PSRs.

Although the Moon is the most studied airless body, there are still many unknowns regarding the regolith properties and composition of the polar regions. One of the biggest unknowns is the amount of water ice available on the Moon, how it is distributed, and its effect on regolith properties. On airless planetary bodies liquid water is not stable, and the stability of water ice depends on the surface temperature. Lunar PSRs are some of the coldest places in the Solar System (Lawrence, 2017; Paige et al., 2010), and if water molecules were delivered or formed there, they would stabilize in the form of ice (Watson et al., 1961). There are many pathways which would result in the presence of water ice in PSRs as summarized in Lawrence (2017). Solar wind implanted hydrogen can form OH, that can migrate to cold traps, where water molecules could be deposited (Lawrence, 2017; Lucey, 2009). Water could also be brought by cometary or volatile-rich asteroid impacts (Lucey, 2009). Finally, water could also be primordial

* Corresponding author at: Lunar Construction Group, Andy Thomas Centre for Space Resources, University of Adelaide, SA 5005, Australia.
E-mail addresses: Karlis.slumba@ucf.edu (K. Šļumba), hannah.sargeant@leicester.ac.uk (H.M. Sargeant), dbritt@ucf.edu (D.T. Britt).
[1] Present address: The University of Leicester, Space Park Leicester, 92 Corporation Rd, Leicester LE4 5SP, UK.

and come from the interior of the Moon (Crotts and Hummels, 2009).

Water ice content in Cabeus crater (84.9°S 35.5°W) was measured directly from the Lunar Crater Observation and Sensing Satellite (LCROSS) impact plume to be $5.6 \pm 2.9 wt.\%$, in addition there were detected many other volatile species (Colaprete et al., 2010). Near-infrared reflectance data acquired by the Moon Mineralogy Mapper (M^3) instrument on Chandrayaan-1 spacecraft are indicative of water ice values up to $30 wt.\%$, but only in some areas of PSRs (Li et al., 2018). Brown et al. (2022) did a large study taking into account results from a total of 8 data sets from Diviner, LAMP, LOLA, M^3, Mini-RF, LEND and LPNS instruments. Averaging over entire PSR areas water ice abundance seems to be clustering below $2 wt.\%$ in PSRs (Brown et al., 2022).

High fidelity simulants are required for many space related fields as a means of testing technologies and experiments in analog environments before launch (e.g., Gaier, 2008). For example, rover wheel performance tests or soil compaction experiments for lunar infrastructure can be conducted in a full-scale regolith bin filled with a simulant that exhibits the correct geophysical properties like particle size, relative density, porosity, etc. It has been pointed out that even minor components of simulants can cause major physical property differences which are of vital importance for certain applications (Gaier, 2008). Simulant characteristics are generally controlled for particle size, shape, and distribution. A key application of simulants is in in-situ resource utilization (ISRU) testing. ISRU is used to harvest useful materials from the local environment. For example, some ISRU techniques are designed to mine volatiles from PSR regolith. Ice mining methods can be partially tested using computer modeling, but these models can only be relied on after they are calibrated with real experimental data. Ice mining methods require regolith simulants that have well simulated mineralogy, geotechnical, and thermal properties (Purrington et al., 2022). Additionally, some properties of simulants are required to test what effect our presence will leave on PSRs, for example, if instruments or humans will heat up regolith enough to release and drive off volatiles (Olthoff et al., 2023).

There are high fidelity dry simulants available for lunar mare and lunar highlands (e.g., Exolith Lab (Long-Fox et al., 2023)), because we have samples returned from the lunar equatorial regions to provide a baseline comparison. It is much more difficult to simulate regolith for lunar PSRs as we have yet to collect and analyze material from these locations to help define the parameters. However, we do know that water ice and other volatiles exist in PSRs (e.g., Colaprete et al., 2010) and that material could have different mechanical and geophysical properties to those found in the equatorial regions (e.g., Sargeant et al., 2020). Although the parameters for PSR regolith are not well-defined, we can use what we do know to help us prepare for initial operations in PSRs where will obtain more crucial information. Currently when a researcher or an engineer requires a PSR simulant to test technologies that are to be used in PSRs, they have to manufacture their own simulant as it is not a readily available product. Individualized production methods lead to differences in properties, and it is therefore challenging to compare and validate results between research teams.

Current PSR simulant production methods can be divided into three types (Fig. 1), see (Ricardo et al., 2023) for an in-depth review of current methods. The first and the simplest approach is the "mud-pie" technique. In this method dry lunar simulant is mixed with water in ambient conditions making a consistency similar to mud. Then this mixture is frozen in a conventional freezer. Liquid water fills the simulant pore space and works as a cement between fine particles, the resulting frozen product has a consistency of concrete with minimal porosity as shown in Fig. 1 A (Gertsch et al., 2006; Metzger et al., 2011; Wasilewski et al., 2021). Compared to dry simulant and other icy simulants produced with alternative techniques, this material exhibits increased mechanical strength (Atkinson and Zacny, 2018; Gertsch et al., 2006; Metzger et al., 2011) and is not a good representation of regolith properties that we expect to find in lunar PSRs. Instead, lunar polar regolith is expected to have high porosity and low cohesion (Gladstone et al., 2012), and potentially decreased bearing capacity (Sargeant et al., 2020).

The second method that has been used to make PSR simulant is to crush ice particles down to fine particle size (10 s to 100 s of microns) and then mechanically mix it with dry lunar simulant (Fig. 1 B) (Dreyer, 2021; Purrington et al., 2022). With this method ice spheres are separate from the mineral grains that make up dry lunar simulant. While there could be granular ice inter-mixed with regolith grains in lunar PSRs, it is predicted that H_2O vapor could collect on the grain surfaces of the cryogenic regolith via vapor deposition in the local vacuum environment. In this scenario, the water ice should be in intimate contact with the other minerals, in other words minerals should be coated with water ice or frost (Cannon and Britt, 2020).

The third method of icy regolith production is designed to replicate H_2O vapor trapping by deposition in a vacuum chamber (Fig. 1 C) (Siegler et al., 2012). A similar method was used in creating high fidelity cometary simulant with amorphous ice and CO_2 inclusions (Bar-Nun and Laufer, 2003). Such a method requires expensive equipment and significant complexity that makes it prohibitive for general users of PSR simulants. There are also challenges with controlling water ice content with this method because the water is deposited in the chamber, and not necessarily on simulant grains. There are more methods for icy simulant production that are not reviewed here, for example, KOmeten SImulation (KOSI) experiments (Grün et al., 1991), that sprayed water – dust mixture into liquid nitrogen. These methods are used when small amounts of simulant are necessary for spectroscopy and to simulate ice phase and volatile or dust inclusions.
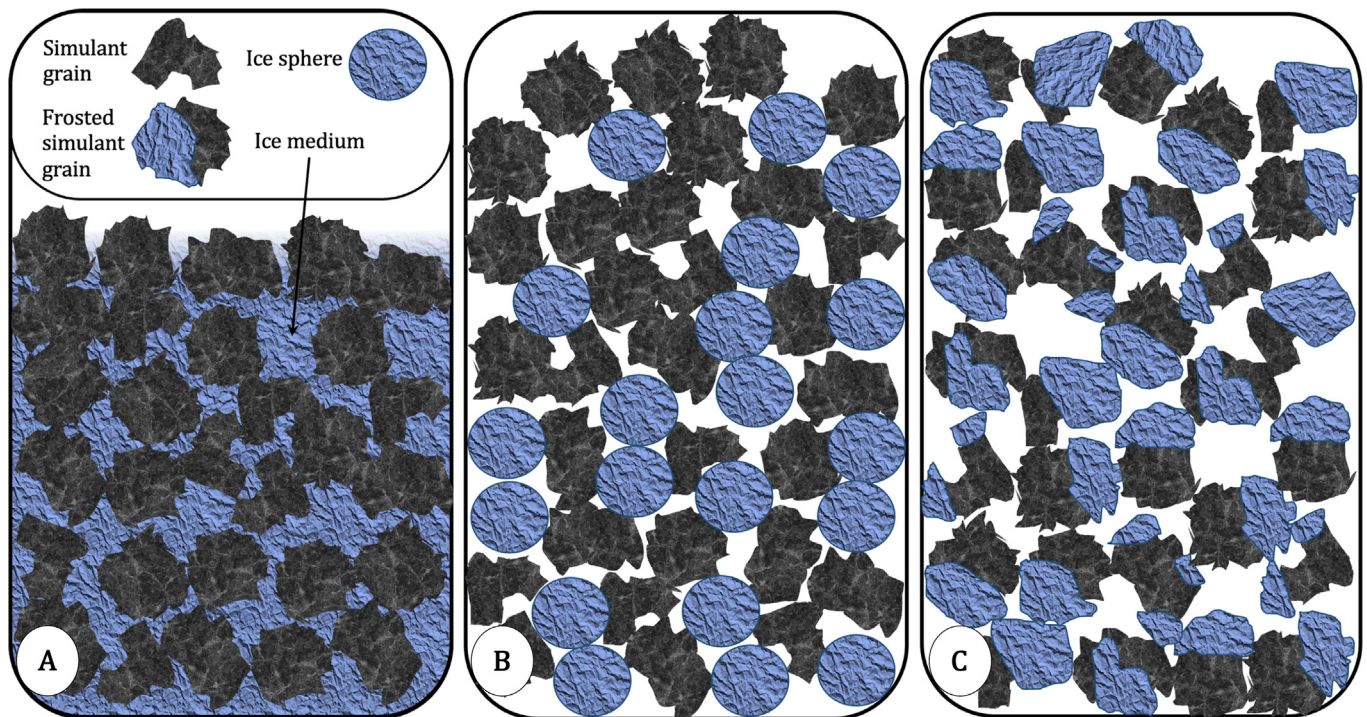
Fig. 1. Three production methods of icy simulants. Image A represents mud-pie method when wet simulant is simply frozen. B is a method where ice spheres are mixed with other mineral grains. C represents vapor deposition where frost is in intimate contact with the other mineral grains.

There are no published techniques that would enable the production of lunar PSR simulant in large batches and with high fidelity, the method reported here will do exactly this. We want our PSR simulant to have high porosity (Gladstone et al., 2012) and low cohesion (mixture has to be granular) (Sargeant et al., 2020; Schultz et al., 2010), and ice should be in intimate contact with other minerals (Cannon and Britt, 2020). It has been hypothesized that regolith in PSRs consists of homogeneous distribution of crystalline ice (Hurley et al., 2012; Metzger et al., 2020). We want to also simulate this homogeneous distribution, so it should be well mixed. It is likely that there are other species of ice present in lunar PSRs, and there could be inclusions of other elements inside the amorphous part of the ices. We are not trying to simulate the trace elemental composition of the ice which likely include small amounts of toxic volatile species, so only deionized water is considered in this work.

The lunar surface can be roughly divided into the lunar highlands and mare. Lunar polar regions are dominated by lunar highlands type regolith (e.g., Lemelin, Lucey, and Camon, 2022). In this project, we use Lunar Highlands Simulant (LHS-1) (Long-Fox et al., 2023) as the base for the PSR simulant. The simulant is made by Exolith Lab, which is a part of the Center for Lunar and Asteroid Surface Science (CLASS).

2. Methods

This section describes our final optimized production setup as sketched in Fig. 2. The general design concept is:

Dry regolith simulant falls through a chamber as water is sprayed from the sides of the chamber. At the base of the chamber is a tray filled with liquid nitrogen (LN_2) where wet simulant grains fall inside and are instantly frozen. After LN_2 evaporates ice-rich simulant grains remain.

2.1. Production setup

The production setup is a prototype and is built using commercial off-the-shelf (COTS) or 3D printed parts. The assembled production setup is shown in Fig. 3. There are no significant reasons why this production device could not be scaled to increase the production rate of the icy simulant. Some of the practicalities for scaling are outlined in the discussion section. Other regolith simulants could be used, and this setup could be repurposed for any other icy simulant production.

The production setup (Fig. 3) is built within a wooden frame of height 790 mm and width 420 mm. The entire setup consists of several separate systems. At the top of the frame is a simulant flow dispenser and control system, and a vibration and sieving system. A misting system is attached to a transparent plastic tube and is essentially in the middle of the production chamber. A collection system is at the bottom.

2.1.1. Flow dispenser and control system

Simulant flow into the chamber is controlled by depositing consistent quantities of simulant into a vibrating sieve. Simulant is manually placed into a funnel with a base diameter of 24 mm, and a capacity for $\sim$ 500 g of simulant.
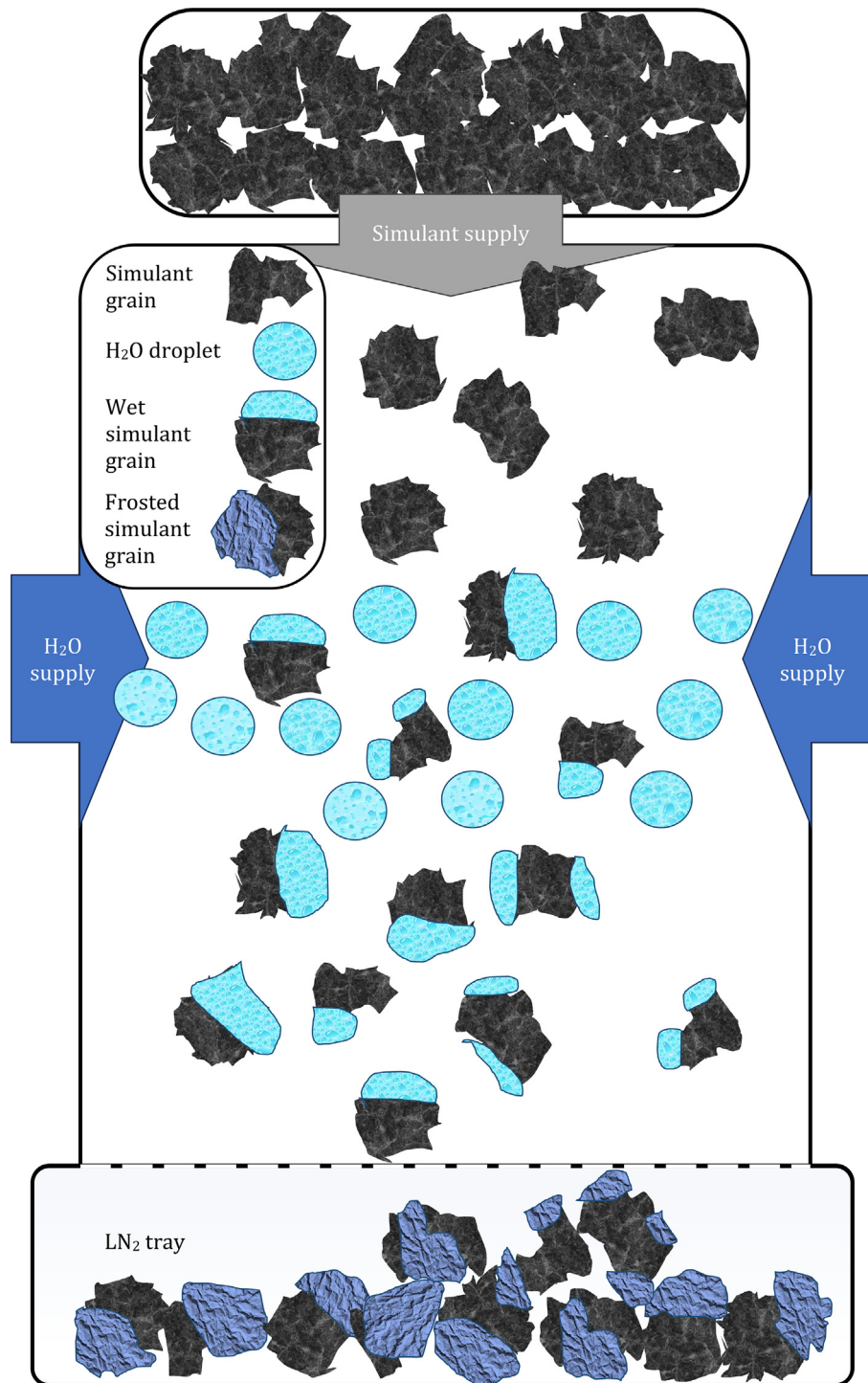
Fig. 2. Simplified icy simulant production scheme. Dry regolith simulant falls through a chamber as water is sprayed from the sides of the chamber. At the base of the chamber is a tray filled with liquid nitrogen (LN_2) where wet simulant grains fall inside and are instantly frozen. After LN_2 evaporates icy simulant remains.

A DC motor is used to rotate a 3D printed component made from polylactic acid (PLA) which has 2 evenly spaced holes (diameter 23 mm) which intermittently release simulant through the base of the funnel. Motor power (which controls rotational speed) is provided by a DC voltage controller and AC-DC converter.

2.1.2. Vibration and sieving system

Once through the funnel, the simulant reaches the sieve (diameter 200 mm, 1 mm mesh). The sieve mesh size is larger than all the simulant particles, and is used to provide a controlled flow of simulant while also maintaining the grain size distribution of the simulant. To further slow
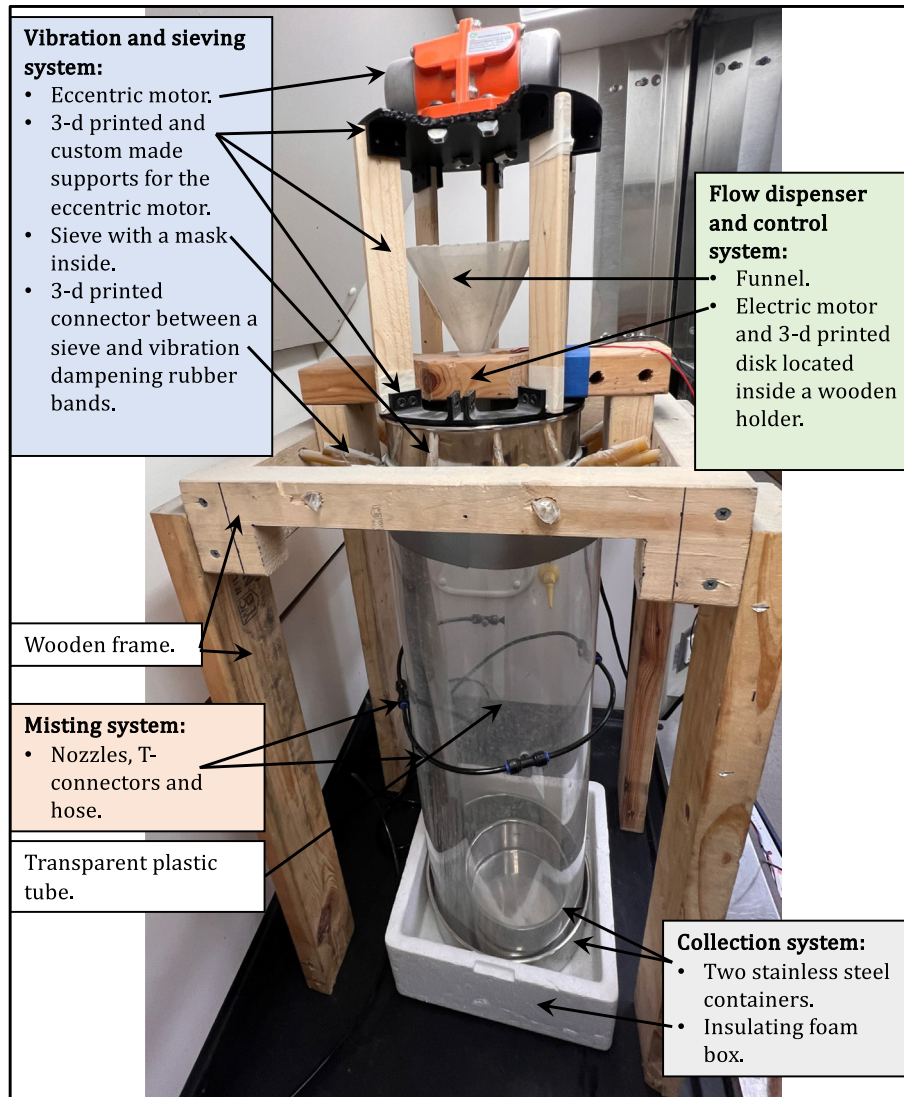
Fig. 3. Production setup. Flow dispenser and control system in green. Vibration and sieving system in blue. Misting system in orange. Collection system in grey.

the simulant flow rate, a 'mask' was added to the sieve (Fig. 4). The mask is 3D printed from PLA and includes 33 holes of 10.5 mm diameter that can be opened or sealed to increase or decrease flow rate respectively. An eccentric electric motor is connected to the sieve with 3D printed holds and wooden supports to agitate the simulant so that it moves through the sieve. The sieve is attached to a 3D printed sieve hold and is held in place to the wooden frame via vibration dampening rubber tubing of 11 mm diameter. The eccentric motor is positioned on supports, so that vibration would not transfer to other systems.

2.1.3. Misting system

Simulant passes through the sieve and falls under gravity through the transparent plastic tube (diameter 241 mm, height 711 mm). The transparent plastic tube was made by rolling an acrylic sheet with the dimensions 711 x 757 x 5 mm. Heating was required to bend this material to the desired shape. The tube has 4 drilled holes where T-connectors with brass misters attach (nozzle diameter 0.5 mm). The misting system is connected with a hose to a deionized water source. Simulant particles falling through the mist become wet and wet grains fall into the collection trays.

2.1.4. Collection system

Wet simulant grains fall into the collection trays (Fig. 5) that are filled with liquid nitrogen (LN_2) and freezes instantly. The stainless steel collection trays both are 75 mm in height with diameters of 152 mm and 241 mm for the small and large trays respectively. A foam (polyethylene) box with inside dimensions 254 x 254 x 108 mm and 19 mm wall thickness is used for thermal insulation and is also filled with LN_2.

Fig. 4. The sieve with 1 mm mesh and the mask with 17 holes open and 16 holes sealed. When the mask is inserted in the sieve, the simulant flow rate can be controlled better by opening or sealing the holes.

Fig. 5. Insulating foam box and two stainless steel containers. During production all containers are filled with liquid nitrogen (LN_2). The plastic tube inserts in the largest stainless steel tray making a production chamber. Largest tray also collects the waste water and residual simulant, that is discarded. Icy simulant is collected in the smallest stainless steel tray.

2.2. Experimental procedure

The first step is to assemble the production setup in the fume hood in ambient conditions as shown in Fig. 3. Setup is built in the fume hood to limit nitrogen build up and for dust mitigation. The production chamber, which includes the transparent tube with misting system, and the collection system, slides under the wooden frame with flow dispenser and control system and vibration and sieving system. The sliding functionality of the production chamber enables convenient LN_2 filling. The foam box and

largest stainless steel container should be filled to 50 % and smallest collection tray to 80 % with LN_2.

The funnel (with the simulant release mechanism closed) can be filled with desired regolith simulant without dismantling the system, in this work 500 g LHS-1 is used for each experiment.

To initiate the simulant flow into the chamber, both motors are started and the hose for water misters is opened. To build up water pressure in the system, the hose is opened a few seconds before the motors are started. Time of the experiment is recorded manually with a stopwatch. When the funnel has been almost emptied of simulant, both motors and water flow are stopped.

The production chamber can be removed from the wooden frame and the transparent plastic tube removed from the collection trays. This requires thermal gloves suitable for LN_2 temperatures. Icy simulant will collect mostly in the smallest collection tray together with leftovers of LN_2. The smallest container with icy simulant is removed from the larger containers. When the remainder of the LN_2 evaporates, the resultant icy simulant collected in the small tray is sieved with a mesh size approximately equivalent to the largest particles of the dry simulant, in this case 1 mm. This is done to make sure that particles are not forming clusters and to have a homogeneous mixture. The sieved icy regolith therefore has a grain size of < 1 mm, and does not account for potential icy regolith containing larger ice grains. The final product can be used for a range of experiments. To avoid further condensation of atmospheric water, the icy simulant should be stored in a dry atmosphere well below the freezing temperature of water, which will also minimize any changes to the ice morphology. The largest collection tray collects waste water and residual simulant, all of this can be discarded.

After production is finished, everything can be disassembled, cleaned, and production can be started again. The leftover LN_2 in the foam box and the simulant in the funnel can be reused. One production round for 500 g of simulant takes ~ 20 min. This process can be repeated immediately to make several kilograms of icy simulant per day and can be scaled-up to much larger production volumes.

2.3. Calibration

Calibration of the production process is necessary to make repeatable icy simulants with consistent water ice concentrations. Two parameters that need to be calibrated are water flow rate and simulant flow rate. If these two are adequately calibrated and all other variables remain constant, then product water ice content can be estimated and repeated.

2.3.1. Running water flow rate

Water flow rate depends on water supply pressure, hose diameter, nozzle diameters and number of nozzles. For this experimental setup only the number of nozzles is variable, and this provides some freedom in changing water flow rate. Here, we measured the flow rate for two nozzles and four nozzles supplying water to the apparatus.

Water pressure from the tap is considered to be constant. Water flow rate was tested in the experimental setup without any simulant present by measuring the mass of water collected in 120 s, equivalent to the timescale for a simulant production run. The average flow rate is calculated by dividing mass of water collected in the smallest container by time the hose was open.

Uncertainty is calculated as one standard deviation (σ) from 3 measurements with this setup. It can be noted from Table 1, that uncertainty is quite significant providing an uncertainty of ~ 20 % of the average value. The most significant factor that influences uncertainty is the location of the collection container in the setup, as the water droplets do not fall with an even distribution in the containers. This experimental setup could be improved so that smallest collection tray would always be located at exactly the same location, to maintain the distribution of water into the container.

2.3.2. Simulant flow rate

Simulant flow rate can be varied by changing the rotational speed of the electric motor that opens and closes the funnel using a rotating disk with a variable number and size of holes. We calibrated the simulant flow rate in the experimental setup without any water flow by comparing the simulant flow rate using two disks with the only difference being that one of the disks has 2 holes and the other has 1 hole, and the hole sizes are equivalent to the funnel base diameter. Simulant flows faster if there are more holes in the disk, increasing the simulant to water ratio, thus decreasing water ice content of the product. Simulant flow rate is mass of simulant that fell through the system in a given time (Table 2). Simulant flow rate experiments were run until most of the simulant had passed through the funnel, while flow rate would be constant.

Uncertainty is calculated as one standard deviation (σ) from 3 measurements with this setup. It can be noted from Table 2, that uncertainty is quite significant at ~ 15 % of the average value. There are several factors that influence the flow rate consistency. There is a gap between the 3D printed disk and the funnel which can affect the amount of simulant lost to the flow dispenser system. This gap should stay constant, but it does change with wear. This gap may vary and should be reevaluated after changing the disk.

3. Analysis

3.1. Water ice content

With the current setup, both simulant flow rate and water flow rate can be varied to control the water/simulant ratio, i.e. the water ice content of a PSR simulant. Each can be set so that the water/simulant ratio can be predicted and targeted for specific simulant requests. With the current setup, one production batch can be up to 500 g in weight. This mass includes both simulant and ice. Water ice content is measured as weight percentage.

To determine how controllable the water ice content of a batch is, a series of experiments were performed. Icy simulants were produced following the procedure in section 2.2, varying the water and simulant flow rates as defined by Proc 1 and Proc 2. For Proc 1, water flows from two nozzles that are set at right angle (90°) and simulant flows through a disk with one hole. For Proc 2, water flows from two opposing nozzles (180°) and simulant flows through a disk with two holes. From the calibration, we predicted that Proc 1 will have 1.3 ± 0.4 times higher water ice content as compared to Proc 2, assuming the water flow rate is unaffected by the direction of the nozzles.

Five samples from each batch were collected in 60 mL glass vials. Mass of the sample was measured for the frozen and then dehydrated sample. To remove non-bound water the samples were heated to 110 ℃ for at least 12 h (NASA-STD-1008, 2021). Icy simulant mass m_0 was recorded for

Table 1
Water flow rate in smallest container calibration example.

Number of nozzles	Water flow rate, g/s	σ, g/s
4	0.422	0.083
2	0.133	0.022

Table 2
Simulant flow rate calibration example.

Simulant	Number of disk holes	Flow rate, g/s	σ, g/s
New LHS-1	1	1.675	0.205
New LHS-1	2	2.244	0.345

each sample vial immediately after icy simulant production. Dry simulant mass m_d was recorded after the dehydration. The mass of water ice removed from the sample during the dehydration stage is calculated as $m_{H_2O} = m_0 - m_d$. Water ice/simulant ratio, R, can be calculated by Eq. (1) dividing lost mass of water m_{H_2O} by the dry simulant mass m_d.

$$R = \frac{m_{H_2O}}{m_d} \qquad (1)$$

Water ice weight percentage W is more informative than ratio and is calculated by Eq. (2), dividing evaporated mass by total mass of the icy simulant, and then multiplying by 100 %.

$$W = \frac{m_{H_2O}}{m_0} * 100\% \qquad (2)$$

The uncertainty in the mass measurements is derived from the precision of the mass balance, which is $\Delta m = \Delta m_0 = \Delta m_{H_2O} = 0.02g$.

Weight percentage uncertainty is calculated using both partial differentiation for each measurement and statistical uncertainty for all measurements of the same batch. Measurement uncertainties by partial differentiation methods are calculated using Eq. (3), where ΔW_{m_0} and $\Delta W_{m_{H_2O}}$ are partial weight percentage uncertainties originating from mass measurement uncertainty for icy simulant mass and water ice mass respectively, they are calculated by Eqs. (4) and (5).

$$\Delta W_{measurement} = \sqrt{\Delta W_{m_0}^2 + \Delta W_{m_{H2O}}^2} \qquad (3)$$

$$\Delta W_{m_0} = \frac{\partial W}{\partial m_0} \Delta m_0 = \frac{\partial \frac{m_{H_2O}}{m_0}}{\partial m_0} \Delta m_0 = 2\frac{m_{H_2O}}{m_0^2} \Delta m_0 \qquad (4)$$

$$\Delta W_{m_{H2O}} = \frac{\partial W}{\partial m_{H2O}} \Delta m_{H2O} = \frac{\partial \frac{m_{H_2O}}{m_0}}{\partial m_{H2O}} \Delta m_{H2O} = \frac{1}{m_0} \Delta m_{H2O} \qquad (5)$$

Statistical uncertainty is calculated using standard deviation using Eq. (6), where n is the number of samples from the same batch (n = 5), and $\overline{W}$ is average weight percentage.

$$\Delta W_{STD} = \sqrt{\frac{\sum \left(W - \overline{W}\right)^2}{n-1}} \qquad (6)$$

Total weight percentage uncertainty is calculated with Eq. (7) where the $\overline{\Delta W_{measurement}}$ term is the average value of measurement uncertainties.

$$\Delta W_{total} = \sqrt{\Delta W_{STD}^2 + \overline{\Delta W_{measurement}}^2} \qquad (7)$$

Measurement uncertainty is typically $0.04wt.\% < \Delta W_{measurement} < 0.1wt.\%$ in units of water ice weight percent. Statistical uncertainty describes the homogeneity of the samples from the batch and is typically in the range $0.2wt.\% < \Delta W_{STD} < 1.0wt.\%$. Uncertainty from measurements is negligible compared to statistical uncertainties.

3.2. Volume

Volume is measured both before, V_0, and after dehydrating the simulant, V_d by directly reading volume from $60mL$ containers with a resolution of $5mL$ (Fig. 6). When icy simulant is filled in these sample containers it is not always level, but this does not influence readability of the volume significantly. While it would be possible to level the surface by shaking the samples, we are not doing this to retain the original porosity. Uncertainty for each volume measurement is $5mL$.

3.3. Density and porosity

Porosity, ϕ, is the ratio of empty space inside the material with respect to total volume. Empty space V_{empty} could be air or vacuum. Porosity is calculated in Eq. (8) where $m_{bulk} = m_{grain} + m_{empty} = m_{grain}$, (assuming $m_{empty} \approx 0$ in the case of air), and Eq. (8) can be simplified to Eq. (9).

$$\phi = \frac{V_{empty}}{V_{bulk}} = \frac{V_{bulk} - V_{grain}}{V_{bulk}} = 1 - \frac{V_{grain}}{V_{bulk}} = 1 - \frac{\frac{m_{grain}}{\rho_{grain}}}{\frac{m_{bulk}}{\rho_{bulk}}} = 1 - \frac{\rho_{bulk}}{\rho_{grain}} \qquad (8)$$

$$\phi = 1 - \frac{\rho_{bulk}}{\rho_{grain}} \qquad (9)$$

In our case for a mixture of regolith and ice, average density values must be used. Bulk density ρ_{bulk} can be calculated by dividing mass and volume of the sample with Eq. (10), for icy simulant with Eq. (11) and for dehydrated simulant with Eq. (12).

$$\rho_{bulk} = \frac{m}{V} \qquad (10)$$

$$\rho_{bulk,\,0} = \frac{m_0}{V_0} \qquad (11)$$

$$\rho_{bulk,\,d} = \frac{m_d}{V_d} \qquad (12)$$

Grain density ρ_{grain} is known both for LHS-1 simulant and for water ice, so the average value can be calculated for a known composition. Simulant grain density is defined as $\rho_{grain,LHS-1} = 2.75 \frac{g}{cm^3}$, as taken from ("Exolith LHS-1 fact sheet," 2022). Water ice density is taken as $\rho_{grain,H_2Oice} = 0.917 \frac{g}{cm^3}$. Average grain density is calculated for a known water ice content of the mixture with Eq. (13), where W is water ice weight percent.

$$\overline{\rho_{grain,0}} = \frac{W}{100\%} * \rho_{grain,\,H_2O\,ice} + \left(1 - \frac{W}{100\%}\right) * \rho_{grain,\,LHS-1} \qquad (13)$$

Porosity of the icy simulant is calculated with Eq. (14) and for the dehydrated simulant with Eq. (15).

$$\phi_0 = 1 - \frac{\rho_{bulk,\,0}}{\rho_{grain,\,0}} \qquad (14)$$

$$\phi_d = 1 - \frac{\rho_{bulk,\,d}}{\rho_{grain,\,LHS-1}} \qquad (15)$$

The uncertainty calculation for both density and porosity consider measurement and statistical uncertainties. Measurement uncertainty for bulk density of icy simulant is calculated with Eq. (16), where $\Delta \rho_{bulk,0,m_0}$ and $\Delta \rho_{bulk,0,V_0}$ are partial bulk density uncertainties originating from mass

Fig. 6. Volume is measured directly reading volume from $60mL$ containers with a resolution of $5mL$.

measurement uncertainty and from volume measurement uncertainty respectively, they are calculated by Eqs. (17) and (18).

$$\Delta\rho_{bulk,\ 0,\ measurement} = \sqrt{\Delta\rho_{bulk,\ 0,\ m_0}^2 + \Delta\rho_{bulk,\ 0,\ V_0}^2} \qquad (16)$$

$$\Delta\rho_{bulk,\ 0,\ m_0} = \frac{\partial\rho_{bulk,0}}{\partial m_0}\Delta m_0 = \frac{\partial\frac{m_0}{V_0}}{\partial m_0}\Delta m_0 = \frac{1}{V_0}\Delta m_0 \qquad (17)$$

$$\Delta\rho_{bulk,\ 0,\ V_0} = \frac{\partial\rho_{bulk,0}}{\partial V_0}\Delta V_0 = 2\frac{m_0}{V_0^2}\Delta V_0 \qquad (18)$$

Statistical uncertainty is calculated using standard deviation using Eq. (19), where n is the number of samples from the same batch ($n = 5$), and $\overline{\rho_{bulk,0}}$ is average bulk density of the icy simulant.

$$\Delta\rho_{bulk,\ 0,\ STD} = \sqrt{\frac{\sum\left(\rho_{bulk,\ 0} - \overline{\rho_{bulk,\ 0}}\right)^2}{n-1}} \qquad (19)$$

Total bulk density uncertainty of the icy simulant is calculated with Eq. (20) where the $\overline{\Delta\rho_{bulk,0,measurement}}$ term is the average value of measurement uncertainties.

$$\Delta\rho_{bulk,\ 0,\ Total} = \sqrt{\Delta\rho_{bulk,0,STD}^2 + \overline{\Delta\rho_{bulk,0,measurement}}^2} \qquad (20)$$

Bulk density uncertainty for redried simulant can be calculated in the same way, just using values after redrying.

Porosity measurement uncertainty for icy simulant can be calculated by Eq. (21) and for dehydrated simulant this would be similar, just using values after dehydration.

$$\Delta\phi_{0,\ \overline{\rho_{grain,0}},\ measurement} = \frac{\partial\phi_0}{\partial\rho_{bulk,\ 0}}\Delta\rho_{bulk,\ 0,\ measurement} =$$
$$= \frac{\partial\left(1 - \frac{\rho_{bulk,0}}{\rho_{grain,0}}\right)}{\partial\rho_{bulk,0}}\Delta\rho_{bulk,\ 0,\ measurement} = \frac{\Delta\rho_{bulk,\ 0,\ measurement}}{\overline{\rho_{grain,0}}} \qquad (21)$$

Statistical uncertainty is calculated using standard deviation in the same way as for weight percentage and density. Total uncertainty is also calculated in the same way as for weight percentage and density.

4. Results

The samples produced from the Proc 1 and Proc 2 experimental procedures were analyzed, and the results are shown in Table 3 and Fig. 7. Proc 1 resulted in simulant with a water ice content of $14.0 \pm 1.3wt.\%$, meanwhile Proc 2 resulted in a simulant with a water ice content of $22.6 \pm 1.3wt.\%$. This demonstrates that water ice content can be somewhat controlled with this technique by varying the simulant flow rate. As a comparison to the possible water ice content of actual lunar PSR regolith, water ice content in lunar PSRs could be up to $30wt.\%$ (Li et al., 2018). Meanwhile, the LCROSS impact in a Cabeus crater and its dust plume spectra was consistent with $5.6 \pm 2.9wt.\%$ (Colaprete et al., 2010).

The icy simulants have increased porosities compared to standard LHS-1 with values over 0.60 as can be seen in Table 3 and Fig. 7. Dry LHS-1 has porosity of 0.52 ± 0.05. Porosity in the PSRs were inferred from LCROSS impact to be around 0.70 (Schultz et al., 2010). While there is a difference between dry and icy simulant, there is no significant porosity difference between samples with various water ice contents, suggesting porosity here is an intrinsic product of the production method. Porosity uncertainties for Proc 1 are larger, because samples were smaller, this raised the importance of uncertainty that is coming from volume measurements. While porosity in our simulants increased compared to the dry simulant, it could be even higher in PSRs.

High porosity is responsible for the low bulk density of the icy simulant, which is $0.87 \pm 0.33g/mL$ and $0.90 \pm 0.12g/mL$ for Proc 1 and Proc 2 respectively. Dry LHS-1 had bulk density of $1.40 \pm 0.12g/mL$, which is significantly higher than for icy simulant. The low density of icy simulant is in good agreement with the minimum densities of the lunar regolith as measured from Apollo and Luna samples (Carrier et al., 1991). Minimum densities were measured for samples that were only couple of grams in weight and values in the range between 0.87 ± 0.03 and $1.30g/mL$ were found (Carrier et al., 1991). Relative

Table 3
Water ice weight percentage, density and porosity of icy simulant made following Proc 1 and Proc 2.

No	W, wt.%	ΔW, wt.%	ρ, g/mL	$\Delta\rho$, g/mL	Porosity (ϕ)	$\Delta\phi$
Proc 1 (1)	15.13 %	1.08 %	0.78	0.31	0.68	0.13
Proc 1 (2)	12.57 %	0.77 %	0.97	0.34	0.61	0.14
Proc 1 (3)	14.21 %	0.60 %	0.86	0.32	0.65	0.13
Proc 2 (1)	21.58 %	0.77 %	0.92	0.14	0.60	0.06
Proc 2 (2)	22.21 %	0.23 %	0.89	0.12	0.62	0.05
Proc 2 (3)	24.15 %	0.95 %	0.89	0.11	0.61	0.05
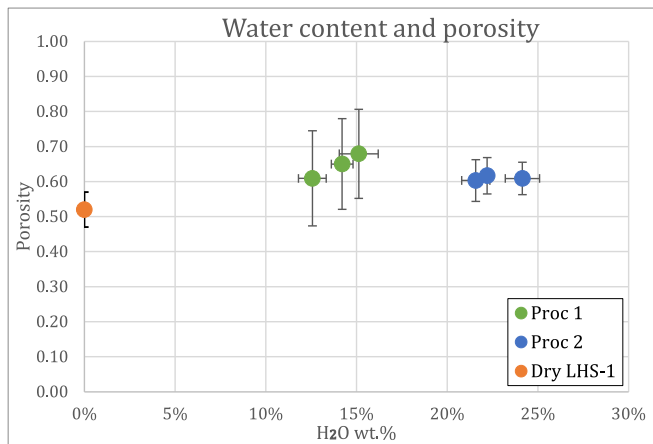
Fig. 7. Porosity and water ice weight percentage of icy simulant from Proc 1 and Proc 2, and from dry LHS-1 for comparison. The icy simulants have increased porosities compared to dry LHS-1.

densities of the icy simulant should be measured for a better comparison.

There is a disagreement between Proc 1 and Proc 2 predictions and results. Proc 1 used only one hole to let simulant fall through, while Proc 2 had two holes. Based on the relative flow rates of water and simulant, we expect Proc 1 to have 1.3 ± 0.4 as much water ice content compared to Proc2. However, Proc 1 has an H_2O content that is 0.62 ± 0.07 times that of Proc 2. The unexpected result may be due to the direction of the nozzles used to supply the water to the system. The two nozzles were located differently, so that they were at 90° in Proc 1 and 180° for Proc 2. This result could be explained by a hydrodynamic anomaly – when water is sprayed from opposite sides $10 \pm 2\%$ of the water ends up in the collection tray, while for a setup when water is sprayed from one side, only $6 \pm 1\%$ of the water is collected. It is assumed that the direction of the nozzles, and therefore the amount of water that reaches the collection tray, is responsible for the discrepancies between the predicted and estimated water ice content for the two procedures. Increased number of misters with smaller nozzles could solve this issue.

Dehydrated simulants maintain higher porosities like the initial icy simulants. However, after handling, shaking or somehow disturbing this 'fairy-castle' structure (Hapke and van Horn, 1963), it collapses to similar porosities as fresh LHS-1 (Fig. 8 and Fig. 9). This could suggest that undisturbed icy regolith that undergoes volatile extraction

could exhibit reduced mechanical strength compared to a regolith which never contained volatiles.

Water ice content homogeneity was tested by taking five samples from each batch and measuring the water ice content of each sample. It can be seen in Table 3 and Fig. 7, that most measurements have small water ice content uncertainties. The water ice content is shown to be homogeneous within each batch. Porosity homogeneity was more difficult to quantify as uncertainties for porosity are much larger in many cases. Porosity uncertainties are largest when samples were smaller and is not believed to be caused by actual discrepancies in porosity between samples from the same batch.

5. Discussion

This experimental setup causes a loss of the finest particles during the production phase. Firstly, finest particles are easily lofted and blown into the dust mitigation system – fume hood. Secondly, fines tend to stick to the wet walls of the production chamber and are washed away. After production the icy simulant is dehydrated in an oven and can be used again as simulant. Such reusability and loss of fines has an impact on the simulant's geotechnical properties as it loses cohesiveness. It is recommended that fresh simulant is used for each batch to ensure a consistent particle size distribution.

It is possible that water might separate from simulant grains upon falling inside the LN_2 tray. If the water separates from simulant grains, then it would form ice spheres like those made with the Setup of Preparation of Icy Planetary Analogues (SPIPA) method, as described in (Yoldi et al., 2015) and their supplementary info. Our hypothesis is that water stays connected to the simulant even after freezing, so that it makes a frost coating. In effect we have water ice and simulant grains in intimate contact. Fresh icy simulant should be observed under a microscope to find out if frost really covers the surface of LHS-1. Observations of this simulant under the microscope were not performed. Such measurement could not be performed within given timeframe because of the nature of the simulant makes such observation difficult without a cryogenic mount in a vacuum chamber. Fresh icy simulant is at LN_2 temperature, approximately 80 K immediately after production. This cold body works as a cold trap for atmospheric water vapor that condenses on the simulant
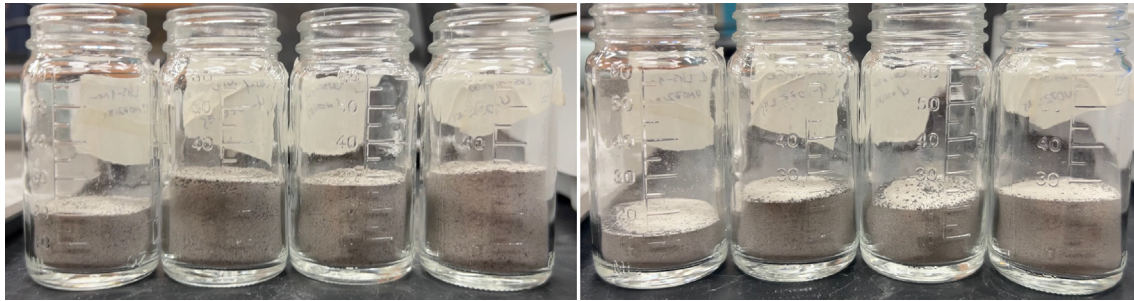
Fig. 8. Left image: Dehydrated simulants. Right image: the same dehydrated simulants after handling. Note volume/porosity collapse.
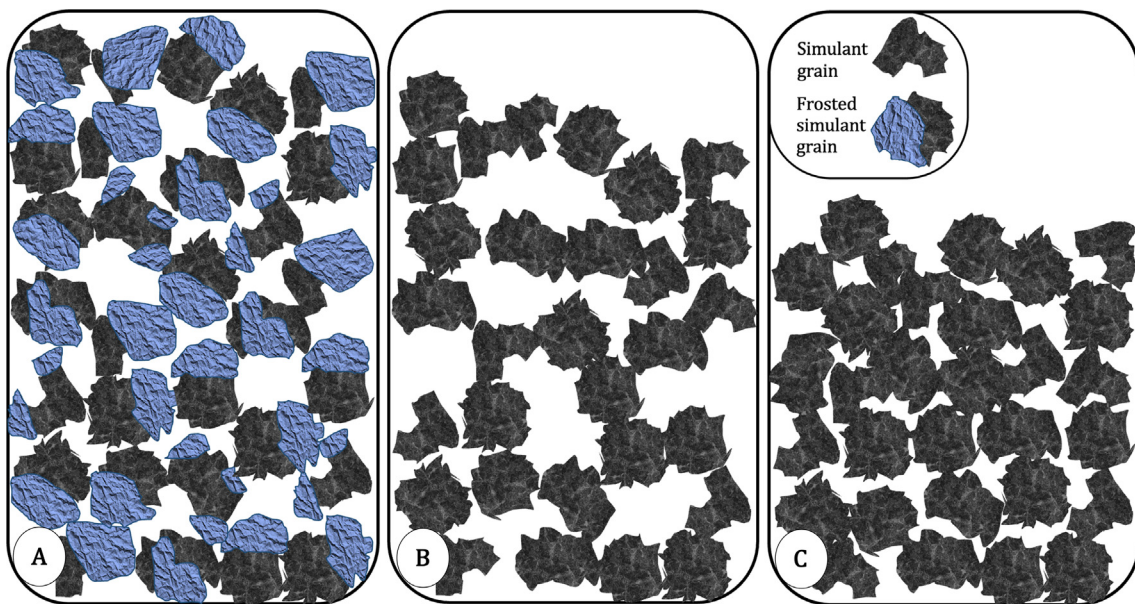

Fig. 9. Diagram demonstrating how dried regolith, that once contained ice, may retain its porosity. Image A: icy simulant. B: Simulant after dehydrating. C: Porosity reduces after handling to equivalent value as fresh LHS-1.

instantly after the production. For a high fidelity analysis such simulant must be produced in a dry atmosphere, but our laboratory setup did not support that at the time of experiment.

This work has demonstrated the concept of icy simulant production with controllable simulant and water flow rates. A second iteration of the design should be built to minimize the highlighted issues and attempt the production of targeted water ice content simulants. Once repeatable batches of icy simulants of controllable water ice content are produced, the simulant and/or the production setup could be used widely by scientists and engineers developing technologies destined for operation in PSR regolith. There are no practical reasons that would limit this setup from being used for production of other icy simulants. For example, Mars and Mercury polar simulants, cometary or Jupiter Trojan asteroid simulants, icy satellite simulants or simulants for outer Solar System bodies. Scaling of the experimental setup should also be possible. For our setup, the fume hood size was the limiting factor of the system size. Other solutions apart from fume hood are possible

for simulant and nitrogen vapor mitigation. If experimental setup could be built in a dry atmosphere, this would limit water condensation on cold surfaces and product. Recommended storage options of the simulant should be explored further, to make sure that simulant doesn't experience any changes during the storage.

6. Conclusions

The goal of the project was to develop a production design for a granular icy regolith simulant of the lunar permanently shadowed regions. This production method is both a simple and low-cost method which still mimics high porosities like those expected in lunar permanently shadowed regions. This setup allows one to make large amounts of icy simulant with homogeneous water ice distribution. This project was a successful proof of concept, and a device for the icy simulant production can be easily replicated as well as it can be upgraded.

The icy simulant with different water ice percentages should be further used for testing water ice content and

porosity effect on physical, thermal, and geotechnical properties of the regolith. While the product should be tested more, the icy simulant already could be used in rudimental experiments for volatile extraction and for robot testing in dirty vacuum chambers.

Main findings:

- The icy simulant has higher porosity than dry simulant. Porosity is between 0.6 and 0.7, similar to what is expected in permanently shadowed regions on the Moon.
- Porosity does not change significantly after dehydrating the simulant, but this fairy castle structure collapses when disturbed. This could suggest that undisturbed icy regolith that undergoes volatile extraction could exhibit reduced mechanical strength.
- The product is homogeneous within each batch, which is up to 500 g with current setup.
- The setup is relatively reliable. Repeating production with the same setup produced icy simulant with water ice content precision of $\pm 1.3\, wt.\%$.

Declaration of competing interest

The authors declare that they have no known competing financial interests or personal relationships that could have appeared to influence the work reported in this paper.

Acknowledgements

References

Atkinson, J., Zacny, K., 2018. Mechanical Properties of Icy Lunar Regolith: Application to ISRU on the Moon and Mars 109–120. https://doi.org/10.1061/9780784481899.012.

Bar-Nun, A., Laufer, D., 2003. First experimental studies of large samples of gas-laden amorphous "cometary" ices. Icarus 161, 157–163. https://doi.org/10.1016/S0019-1035(02)00016-7.

Brown, H.M., Boyd, A.K., Denevi, B.W., Henriksen, M.R., Manheim, M.R., Robinson, M.S., Speyerer, E.J., Wagner, R.V., 2022. Resource potential of lunar permanently shadowed regions. Icarus 377, 114874. https://doi.org/10.1016/j.icarus.2021.114874.

Cannon, K.M., Britt, D.T., 2020. A geologic model for lunar ice deposits at mining scales. Icarus 347, 113778. https://doi.org/10.1016/j.icarus.2020.113778.

Carrier III, W.D., Olhoeft, G.R., Mendell, W., 1991. Physical properties of the lunar surface. In: Lunar Sourcebook, A User's Guide to the Moon. Cambridge University Press, pp. 475–594.

Colaprete, A., Schultz, P., Heldmann, J., Wooden, D., Shirley, M., Ennico, K., Hermalyn, B., Marshall, W., Ricco, A., Elphic, R.C., Goldstein, D., Summy, D., Bart, G.D., Asphaug, E., Korycansky, D., Landis, D., Sollitt, L., 2010. Detection of water in the LCROSS ejecta plume. Science 330, 463–468. https://doi.org/10.1126/science.1186986.

Crotts, A.P.S., Hummels, C., 2009. LUNAR outgassing, transient phenomena, and the return to the moon. ii. predictions and tests for outgassing/regolith interactions. ApJ 707, 1506. https://doi.org/10.1088/0004-637X/707/2/1506.

Dreyer, C.B., 2021. Mining lunar polar ice for LO2/LH2 propellant. Presented at the ASCEND 2021. https://doi.org/10.2514/6.2021-4235.

Exolith LHS-1 fact sheet [WWW Document], 2022. URL https://cdn.shopify.com/s/files/1/0398/9268/0862/files/lhs-1-spec-sheet-Dec2022.pdf?v=1670609567 (accessed 2.1.23).

Gaier, J., 2008. The Need for High Fidelity Lunar Regolith Simulants (No. NASA/TM—2008-215261).

Gertsch, L., Gustafson, R., Gertsch, R., 2006. Effect of water ice content on excavatability of lunar regolith. AIP Conference Proceedings 813, 1093–1100. https://doi.org/10.1063/1.2169290.

Gladstone, G.R., Retherford, K.D., Egan, A.F., Kaufmann, D.E., Miles, P.F., Parker, J.W., Horvath, D., Rojas, P.M., Versteeg, M.H., Davis, M.W., Greathouse, T.K., Slater, D.C., Mukherjee, J., Steffl, A.J., Feldman, P.D., Hurley, D.M., Pryor, W.R., Hendrix, A.R., Mazarico, E., Stern, S.A., 2012. Far-ultraviolet reflectance properties of the moon's permanently shadowed regions. J. Geophys. Res. Planets 117. https://doi.org/10.1029/2011JE003913.

Grün, E., Kochan, H., Seidensticker, K.J., 1991. Laboratory simulation, a tool for comet research. Geophys. Res. Lett. 18, 245–248. https://doi.org/10.1029/90GL02522.

Hapke, B., van Horn, H., 1963. Photometric studies of complex surfaces, with applications to the moon. J. Geophys. Res. 1896–1977 (68), 4545–4570. https://doi.org/10.1029/JZ068i015p04545.

Hurley, D.M., Lawrence, D.J., Bussey, D.B.J., Vondrak, R.R., Elphic, R.C., Gladstone, G.R., 2012. Two-dimensional distribution of volatiles in the lunar regolith from space weathering simulations. Geophys. Res. Lett. 39. https://doi.org/10.1029/2012GL051105.

Lawrence, D.J., 2017. A tale of two poles: Toward understanding the presence, distribution, and origin of volatiles at the polar regions of the moon and mercury. J. Geophys. Res. Planets 122, 21–52. https://doi.org/10.1002/2016JE005167.

Lemelin, M., Lucey, P.G., Camon, A., 2022. Compositional maps of the lunar polar regions derived from the kaguya spectral profiler and the lunar orbiter laser altimeter data. Planet. Sci. J. 3, 63. https://doi.org/10.3847/PSJ/ac532c.

Li, S., Lucey, P.G., Milliken, R.E., Hayne, P.O., Fisher, E., Williams, J.-P., Hurley, D.M., Elphic, R.C., 2018. Direct evidence of surface exposed water ice in the lunar polar regions. Proc. Natl. Acad. Sci. 115, 8907–8912. https://doi.org/10.1073/pnas.1802345115.

Long-Fox, J.M., Landsman, Z.A., Easter, P.B., Millwater, C.A., Britt, D.T., 2023. Geomechanical properties of lunar regolith simulants LHS-1 and LMS-1. Adv. Space Res. https://doi.org/10.1016/j.asr.2023.02.034.

Lucey, P.G., 2009. The poles of the moon. Elements 5, 41–46. https://doi.org/10.2113/gselements.5.1.41.

Metzger, P.T., Galloway, G.M., Mantovani, J.G., Zacny, K., Zacny, Kris, Craft, J., 2011. Low force icy regolith penetration technology (No. NASA/TM-2011-216302).

Metzger, P.T., Zacny, K., Morrison, P., 2020. Thermal extraction of volatiles from lunar and asteroid regolith in axisymmetric crank-nicolson modeling. J. Aerosp. Eng. 33, 04020075. https://doi.org/10.1061/(ASCE)AS.1943-5525.0001165.

NASA-STD-1008, 2021. Classifications and requirements for testing systems and hardware to be exposed to dust in planetary environments. https://standards.nasa.gov/standard/NASA/NASA-STD-1008.

Olthoff, C., Kaschubek, D., Killian, M., 2023. Dynamic thermal interactions between spacesuits and lunar regolith in permanently shaded regions on the moon. Acta Astronaut. 203, 351–369. https://doi.org/10.1016/j.actaastro.2022.12.001.

Paige, D.A., Siegler, M.A., Zhang, J.A., Hayne, P.O., Foote, E.J., Bennett, K.A., Vasavada, A.R., Greenhagen, B.T., Schofield, J.T., McCleese, D.J., Foote, M.C., DeJong, E., Bills, B.G., Hartford, W., Murray, B.C., Allen, C.C., Snook, K., Soderblom, L.A., Calcutt, S., Taylor, F.W., Bowles, N.E., Bandfield, J.L., Elphic, R., Ghent, R., Glotch, T.D., Wyatt, M.B., Lucey, P.G., 2010. Diviner lunar radiometer observations of cold traps in the moon's south polar region. Science 330, 479–482. https://doi.org/10.1126/science.1187726.

Purrington, C., Sowers, G., Dreyer, C., 2022. Thermal mining of volatiles in lunar regolith simulant. Planet. Space Sci. 222, 105550. https://doi.org/10.1016/j.pss.2022.105550.

Ricardo, D., Hodgkinson, J., Akbar Rhamdhani, M., Brooks, G., 2023. A review on the preparation techniques and geotechnical behaviour of icy lunar regolith simulants. Adv. Space Res. https://doi.org/10.1016/j.asr.2023.09.032.

Sargeant, H.M., Bickel, V.T., Honniball, C.I., Martinez, S.N., Rogaski, A., Bell, S.K., Czaplinski, E.C., Farrant, B.E., Harrington, E.M., Tolometti, G.D., Kring, D.A., 2020. Using Boulder Tracks as a Tool to Understand the Bearing Capacity of Permanently Shadowed Regions of the Moon. J. Geophys. Res. Planets 125, e2019JE006157. https://doi.org/10.1029/2019JE006157.

Schultz, P.H., Hermalyn, B., Colaprete, A., Ennico, K., Shirley, M., Marshall, W.S., 2010. The LCROSS cratering experiment. Science 330, 468–472. https://doi.org/10.1126/science.1187454.

Siegler, M., Aharonson, O., Carey, E., Choukroun, M., Hudson, T., Schorghofer, N., Xu, S., 2012. Measurements of thermal properties of icy Mars regolith analogs. J. Geophys. Res. Planets 117. https://doi.org/10.1029/2011JE003938.

Wasilewski, T.G., Barciński, T., Marchewka, M., 2021. Experimental investigations of thermal properties of icy lunar regolith and their influence on phase change interface movement. Planet. Space Sci. 200, 105197. https://doi.org/10.1016/j.pss.2021.105197.

Watson, K., Murray, B.C., Brown, H., 1961. The behavior of volatiles on the lunar surface. J. Geophys. Res. 1896–1977 (66), 3033–3045. https://doi.org/10.1029/JZ066i009p03033.

Yoldi, Z., Pommerol, A., Jost, B., Poch, O., Gouman, J., Thomas, N., 2015. VIS-NIR reflectance of water ice/regolith analogue mixtures and implications for the detectability of ice mixed within planetary regoliths. Geophys. Res. Lett. 42, 6205–6212. https://doi.org/10.1002/2015GL064780.